

DOI: 10.1002/ ((please add manuscript number))

Article type: Full Paper

Enhanced Interfacial Stability of Hybrid-Electrolyte Lithium-Sulfur Batteries with a Layer of Multifunctional Polymer with Intrinsic Nanoporosity

*Xingwen Yu and Arumugam Manthiram**

Dr. X. Yu and Prof. A. Manthiram

Materials Science & Engineering Program and Texas Materials Institute, The University of Texas at Austin, Austin, TX78712, USA

E-mail: manth@austin.utexas.edu

Keywords: lithium-sulfur batteries, solid electrolyte, polymer with intrinsic nanoporosity, electrode-electrolyte interface, lithium polysulfide

Abstract: The use of lithium-ion conductive solid electrolytes offers a promising approach to address the polysulfide-shuttle and the lithium-dendrite problems in lithium-sulfur (Li-S) batteries. One critical issue with the development of solid-electrolyte Li-S batteries is the electrode-electrolyte interfaces. We present herein a strategic approach by employing a thin layer of a polymer with intrinsic nanoporosity (PIN) on a Li⁺-ion conductive solid electrolyte, which significantly enhances the ionic interfaces between the electrodes and the solid electrolyte. Among the various types of Li⁺-ion solid electrolytes, NASICON-type Li_{1+x}Al_xTi_{2-x}(PO₄)₃ (LATP) offers advantages in terms of Li⁺-ion conductivity, stability in ambient environment, and practical viability. However, LATP is susceptible to reaction with both the Li-metal anode and polysulfides in Li-S batteries due to the presence of easily reducible Ti⁴⁺ ions in it. The coating with a thin layer of PIN presented in this study overcomes the above issues. At the negative-electrode side, the PIN layer prevents the direct contact of Li-metal with the LATP solid electrolyte, circumventing the reduction of LATP by Li metal. At the positive electrode side, the PIN layer prevents the migration of polysulfides to the surface of LATP, preventing the reduction of LATP by polysulfides.

1. Introduction

Electrochemical energy storage technologies with rechargeable batteries are crucial for a broad range of applications including mobile electronics, electric vehicles, and stationary large-scale electricity grids.^[1] The market of portable power sources is dominated by lithium-ion (Li^+ -ion) batteries, which are appealing for electric vehicles and grid storage as well.^[2] However, the relatively low capacity of the traditional insertion-type positive electrode materials strictly restrains the overall energy density of Li^+ -ion batteries.^[3] Targeting the enhancement of energy density, batteries with a lithium-sulfur (Li-S) chemistry provide a compelling blueprint and have recently received overwhelming attention.^[4] Sulfur is an earthly abundant element, which yields an exceptionally high theoretical gravimetric capacity of $1,672 \text{ mA h g}^{-1}$. However, although many efforts and endeavor have been made over the past years, critical obstacles in the Li-S battery technologies still persist and need to be overcome.

One of the most crucial problems toward the implementation of practicable Li-S technologies is the so-called “polysulfide-shuttle” issue.^[5] The reduction of elemental sulfur to lithium sulfide experiences a series of polysulfide species that are soluble in the nonaqueous electrolytes used. During the operation of a Li-S cell, the dissolved polysulfide species have a tendency to transport from the positive electrode to the negative electrode through the porous polymeric separator and chemically react with the Li-metal. As a result, the shuttling of polysulfides induces capacity degradation caused by the loss of sulfur at the cathode.^[6] A lot of efforts have been made over the past few years for encapsulating the polysulfides within the positive electrode. Most of the attempts have been focused on the development of advanced cathode matrices.^[7] However, with porous separators, only focusing on the advancement of cathode structures is not able to fully overcome the polysulfide shuttle.

Use of Li^+ -ion conductive solid electrolytes provides a promising prospect for circumventing the polysulfide migration problem.^[8] The progress in solid-electrolyte Li-S

batteries has recently been comprehensively reviewed.^[9] One strategy is the development of all solid-state Li-S batteries.^[10] However, due to the high impedance at the electrode/electrolyte interface, the all solid-state Li-S batteries suffer a sequence of obstacles in terms of the low utilization of active material and short cycle life etc.^[11] As a matter of fact, due to the unique electrochemical processes of the Li-S chemistry, it is generally realized that the liquid nonaqueous electrolyte is essential to facilitate Li⁺-ion transport through the formation of soluble polysulfides during the operation of Li-S batteries.^[12] Accordingly, a hybrid-electrolyte Li-S battery concept has recently been proposed and demonstrated by employing a Li⁺-ion solid electrolyte serving as both a separator and as a Li⁺-ion transport medium to maintain ionic charge transfer between the anode and the cathode.^[13] Meanwhile, a nonaqueous liquid electrolyte is employed to facilitate the transition reactions at the sulfur cathode. With this approach, a NASICON-type solid electrolyte Li_{1+x}Al_xTi_{2-x}(PO₄)₃ (LATP) was primarily employed. We have also previously proposed a Li_{1+x}Y_xZr_{2-x}(PO₄)₃ (LYZP) solid electrolyte for the development of hybrid-electrolyte Li-S batteries.^[8b] However, the ionic conductivity of LYZP was only *ca.* one-tenth of that of LATP. As a matter of fact, among the various types of Li⁺-ion solid electrolytes, the NASICON-type LATP exhibits multiple advantages in terms of Li⁺-ion conductivity, stability in ambient atmosphere, and practical viability.^[14] However, the spontaneous reaction of LATP with Li metal and the facile reduction of Ti⁴⁺ by polysulfides, as well as its relatively narrow electrochemical stability window lead to a series of crucial chemical/electrochemical-incompatibility problems of LATP in Li-S cells.^[15] In addition, it is very difficult to develop an ideal ionic interface between the solid electrolyte and the Li-metal, restraining the overall cell performance.^[16]

Herein, we present a strategical approach to overcome the above problems by employing a thin layer of a polymer with intrinsic nanoporosity (PIN) on the LATP solid electrolyte. The PIN layer prevents direct contact of the LATP membrane with the electrodes (both the Li-metal anode and the sulfur/polysulfide cathode). The PIN also serves as an

electrically insulating layer to prevent the LATP from being electrochemically reduced during the operation of the cell. Moreover, the PIN layer can provide a facile Li⁺-ion transport path at the interface of Li-metal anode/LATP solid electrolyte.

2. Results and Discussion

The synthesis of a polymer with intrinsic nanoporosity (PIN) was achieved through a reaction between tetrafluoroterephthalonitrile and tetrahydroxy-3,3,3',3'-tetramethyl-1,1'-spirobisindane,^[17] as described in the experimental section. The yielded PIN was yellow powder with a molecular structure as illustrated in **Figure 1a**. The synthesized PIN material was first analyzed with nuclear magnetic resonance spectroscopy (NMR). The ¹H NMR spectrum of this material provided in Figure 1b is consistent with the expected structure of the PIN polymer. A Fourier transform infrared (FTIR) spectrum of the synthesized PIN material is presented in Figure 1c. The C–H bending peak of –CH₂– group is located at 2840 – 2960 cm⁻¹, while the bending peak of C–H species related to the C–CH₃ groups is located at 1456 cm⁻¹. The C–O stretching peaks owing to the aromatic–O–aromatic (Ar–O–Ar) groups are located at 1000–1300 cm⁻¹. The peak at 1607 cm⁻¹ is attributed to the aromatic bending of C=C, while the C≡N bending peak is at 2238 cm⁻¹. The PIN material exhibits amorphous feature as reflected by the X-ray diffraction (XRD) pattern (Figure 1d). A commercially available LATP membrane (Li_{1+x}Al_xTi_{2-x}(PO₄)₃, supplied by OHARA Inc., Japan, as pictured in **Figure S1a**) with the typical NASICON structure as illustrated in **Figure 2a** and as reflected by the XRD pattern in Figure 2b was employed for this study. The Li⁺-ion conductivity of this material is *ca.* 1×10⁻⁴ S cm⁻¹ (provided by the supplier) at room temperature. The PIN thin layer on the LATP membrane was developed by a dip-coating process, which is detailed in the experimental section. The LATP membrane was coated on both sides. A PIN-coated LATP membrane is pictured in Figure S1b. The XRD pattern of the PIN-coated LATP is presented in Figure 2c. There is no difference between the uncoated and

the coated LATP (Figure 2b and c), indicating a good compatibility between the PIN and the LATP membrane (*i.e.*, no reactions occur during the coating process). Figure 2d shows a scanning electron microscope (SEM) image of the cross-section of the PIN-coated LATP, from which it can be seen that the PIN is firmly adhered onto the surface of the LATP membrane. The bonding of PIN on the surface of LATP is presumed to be through a mechanical anchoring and inter-hooking mechanism, as in other polymer/ceramic interfaces.^[18] 3D noncontact Profilometer measurement suggests that the thickness of the PIN coating is *ca.* 20 – 25 μm (Figure 2e and f). **Figure S2a** and b show the scanning electron microscope (SEM) images of the uncoated and PIN-coated LATP membranes. The LATP membrane shows a smooth surface with scattered dents (Figure S2a). The PIN coating exhibits a uniform and dense morphology (Figure S2b).

How to maneuver an appropriate interface between the electrolyte and electrodes has always been a challenge in developing solid-electrolyte batteries.^[19] In fact, in an electrochemical system, it has invariably been difficult to develop a desirable ionic path at the interface of a ceramic electrolyte and a metal electrode. The same problem exists in Li-S batteries with a solid electrolyte as well. Application of a malleable polymer interlayer between the solid electrolyte and the electrodes offers an ideal buffer interface to enhance the interfacial contact between the hard surfaces of the ceramic electrolyte and metal electrodes. The PIN coating on the LATP first acts as such a functional buffer layer. A small amount of liquid electrolyte ($\text{LiCF}_3\text{SO}_3/\text{DME-DOL}$) absorbed in the PIN provides an effective ionic interface for the transport of Li^+ -ions between the Li-metal electrode and the LATP solid electrolyte. The PIN coated LATP membrane was first evaluated in a Li-Li symmetric cell prepared with Li-metal electrodes at each side of the membrane, as schematically illustrated in **Figure S3**. For a comparison, a Li-Li symmetric cell with an uncoated LATP membrane was tested as well. The cell assembly details are described in the experimental section. **Figure 3a** and b present the voltage responsive profiles of the Li-Li symmetric cells with,

respectively, an uncoated and a PIN coated LATP membranes. With the uncoated LATP membrane, the symmetric cell exhibits a bumpy voltage profile with a relatively high overpotential (Figure 3a). Moreover, the overpotential increases continuously with prolonged cycling. However, with the PIN coated LATP membrane, the symmetric cell shows high overpotential in the first cycle, which is speculated to be attributed to the preconditioning of the cell, then the voltage feedback becomes smooth and stable at a relatively low level (Figure 3b, consecutive voltage/current profile during the first 200 h of operation). Apparently, the PIN coating significantly enhances the interfacial property between the Li-metal and the LATP solid electrolyte. The 1,000-hour voltage/current profile of the Li || PIN-LATP || Li symmetric cell is provided in **Figure S4**. It is noticeable that the voltage gap between the charge and discharge profiles starts to slightly increase after *ca.* 800 h. The increase in the over potential of the Li || PIN-LATP || Li symmetric cell is most likely attributed to the consumption of the liquid electrolyte at the Li/PIN/LATP interface.

Li-S coin cells with the PIN-coated LATP were assembled with a Li-foil anode and a carbon/sulfur cathode, as detailed in the experimental section and as schematically illustrated in **Figure S5**. The cell is annotated as Li || PIN-LATP || S/C. For a comparison, control Li-S cells were prepared with an uncoated LATP membrane (annotated as Li || LATP || S/C cell). Figure 3c and d compare the discharge-charge profiles of the two cells in the first several cycles. At a moderate C-rate (C/10), the Li || LATP || S/C cell is operable at the beginning but the voltage profile is very bumpy. At high C-rates, the Li || LATP || S/C cell is not operable. For the Li || PIN-LATP || S/C cell (Figure 3d), the smooth voltage profile and the reasonable discharge-charge voltages reveal that a facile ionic interface has been successfully realized with the assistance of the PIN coating.

Figure 4 presents electrochemical characteristics and cycling performances of the Li || PIN-LATP || S/C cells. For a comparison, a series of regular Li-S cells prepared with Celgard separators were also tested under the same conditions. The Celgard-separator cells are termed

as Li || Celgard || S/C. In order to give a direct and clear comparison between the solid-electrolyte separator and the Celgard separator, all the Li-S cells (either the Li || PIN-LATP || S/C or the Li || Celgard || S/C cells) were assembled with a simple cathode configuration without any additional components (*e.g.*, a carbon interlayer that is able to assist for the suppression of polysulfide migration)^[20] being applied to the cathode. Figure 4a compares the cyclic voltammograms (CVs) of a Li || PIN-LATP || S/C and a Li || Celgard || S/C cell. The Li || PIN-LATP || S/C cell also exhibits two reduction waves in the cathodic process and one overlapped oxidation wave in the anodic process similar to the Li-S cells with a Celgard separator. However, in contrast to the Li || Celgard || S/C cell, the presence of PIN-LATP solid electrolyte shifts the cathodic waves a little bit to the left (towards lower voltage) and the anodic peak a little bit to the right (towards higher voltage). Additionally, a less sharp feature of the peaks are observed for the Li || PIN-LATP || S/C cell during both the cathodic and anodic scans. The difference in the CV behavior between the two cells is presumably due to the variations of the Li⁺-ion transport in the different electrolytes. The kinetics of Li⁺-ion transport is supposed to be more facile in the liquid electrolyte than that in the solid electrolyte.

Figure S6 compares charge-discharge profiles of the Li || PIN-LATP || S/C cell and the Li || Celgard || S/C cell at the same rate of C/10. Consistent with the results reflected from Figure 4a, the Li || PIN-LATP || S/C cell shows a lower discharge voltage and a higher charge voltage than the Li || Celgard || S/C cell, implying a relatively sluggish Li⁺-ion transport in the ceramic solid electrolyte. Figure 4b shows the rate capability of the Li || PIN-LATP || S/C cell. The cells can deliver reasonably high specific capacity at reasonable cycling rates as summarized in **Table 1**. Charge-discharge curves of a series Li || Celgard || S/C cells at various cycling rates are presented in **Figure S7**. Due to the relatively lower ionic conductivity of the solid electrolyte, the Li || PIN-LATP || S/C cells exhibit relatively higher voltage polarization

relative to that of the Li || Celgard || S/C cell when they are cycled at the same C rates (Table 1).

Figure 4c compares the long-term cycling of the Li || PIN-LATP || S/C cell and the Li || Celgard || S/C cell at the same cycling rate of C/5. Apparently, the Li || PIN-LATP || S/C cell shows significant advantages over the Li || Celgard || S/C cell with respect to capacity retention with prolonged cycling. Although the Li || PIN-LATP || S/C cell delivers relatively lower initial discharge capacity than the Li || Celgard || S/C cell, after *ca.* 50 charge-discharge cycles, the specific capacity of the Li || PIN-LATP || S/C cell exceeds that of the Li || Celgard || S/C cell. After *ca.* 70 cycles, there appear a sharp capacity decline for the Li || Celgard || S/C cell. However, for the Li || PIN-LATP || S/C cell, *ca.* 800 mA h g⁻¹ was maintained after 150 cycles. Noticeably, throughout the 200 cycles, the Li || PIN-LATP || S/C cell shows marginally higher Coulombic efficiency than the Li || Celgard || S/C cell. Figure 4d presents the Nyquist plots of electrochemical impedance spectra (EIS) of the Li || PIN-LATP || S/C cell after being cycled for different number of cycles. For a nonaqueous alkali metal (Li, Na, or K) - sulfur battery, the EIS behavior can be generally expressed with an equivalent circuit as shown in **Figure S8**.^[21] The bulk impedance R_L in Figure S8 can be determined from the real axis value at the high frequency intercept in Figure 4d. The charge-transfer impedance R_{ct} in Figure S8 can be determined from the diameter of the semicircle at the low frequency in Figure 4d. The bulk impedance R_L does not change too much during cell cycling, but the charge-transfer impedance R_{ct} varies a lot. The cell exhibits a relatively large R_{ct} value before cycling, which is likely due to a self-conditioning issue of a freshly prepared cell. After one cycle, the cell exhibits a small R_{ct} . Afterward, the R_{ct} value increases continuously with prolonged cycling, which is likely due to the continuous loss of contact between the sulfur/sulfide/polysulfide and the carbon matrices.

The use of LATP solid electrolyte is to circumvent the polysulfide shuttle problem during the operation of Li-S batteries. Such an effect can also be reflected by the deterioration

of the Li-metal anode after cycling the cells. **Figure 5a** and b displays the surface morphologies of the cycled lithium-metal anodes removed from, respectively, the Li || Celgard || S/C cell and the Li || PIN-LATP || S/C cell. As expected, the cycled Li-metal electrodes exhibit rough surfaces. However, in contrast, the unevenness of the Li-metal anode from the Li || Celgard || S/C cell is much more serious due to the reaction of Li-metal with the shuttled polysulfide species.^[22] This fact further confirms that the polysulfide migration has been effectively suppressed by the solid electrolyte.

It has been previously demonstrated that the LATP solid electrolyte exhibits chemical incompatibility with polysulfides due to the reduction of Ti^{4+} by the polysulfide species.^[15b] In this study, a Li-S cell was prepared with an uncoated LATP solid electrolyte. To ensure the cyclability of the cell, a piece of Celgard membrane was placed in between the Li-foil anode and the LATP membrane. In addition, another piece of Celgard membrane was placed in between the sulfur cathode and the LATP membrane. The Celgard membranes were pre-soaked with a regular liquid electrolyte (trifluoromethanesulfonate dissolved in a mixture of dimethoxyethane and 1,3-dioxolane, $\text{LiCF}_3\text{SO}_3/\text{DME-DOL}$). The assembly of such a cell is as schematized in **Figure S9**. In such a cell, the liquid electrolyte ($\text{LiCF}_3\text{SO}_3/\text{DME-DOL}$) soaked Celgard membrane prevents the direct contact of the Li-foil anode with the LATP membrane and can provide an effective ionic interface between the Li-metal electrode and the LATP solid electrolyte, thus ensuring the cyclability of the cell. However, at the cathode side, the LATP membrane is exposed to the polysulfide-rich environment during cell operation since polysulfide can penetrate the Celgard membrane and reach the surface of LATP. The cell was disassembled after 30 cycles and the LATP membrane was found to turn into blue color (**Figure S10**) due to the reduction of Ti^{4+} to Ti^{3+} in the LATP by the polysulfide species.

Figure 5c and d compare the pore morphologies of the Celgard membrane and the PIN membrane. The pore size of the Celgard is generally in the micrometer scale that inevitably allows polysulfide species to easily transport through. Therefore, with the application of a

piece of Celgard membrane between the sulfur cathode and the LATP membrane, the polysulfide species are still able to access the surface of LATP and induces chemical reaction between the LATP and the polysulfides. On the other hand, as shown in Figure 5d, the PIN exhibits an almost nonporous feature. In fact, the pore size of the PIN material is difficult to be characterized with microscopic techniques. Therefore, we have previously estimated the pore dimension of the PIN by means of combined simulation/experimental methodologies (molecular dynamic calculation/x-ray scattering).^[17] The pores of PIN have a diameter of < 1.0 nm. Such pore-dimension can efficaciously prevent the migration of polysulfide species, but allows the transport of Li⁺ ions. With its unique pore structure, the PIN coating can provide an effective shield to protect the LATP membrane from being in direct contact with the polysulfide species. **Figure S11** shows a picture of a piece of PIN-coated LATP after being cycled for 150 times in a Li || PIN-LATP || S/C cell. There is no color change of the LATP membrane. Figure 6a shows the XRD pattern of a cycled PIN-coated LATP membrane (after 150 cycles in a Li || PIN-LATP || S/C cell). There is no difference observed between the XRD patterns shown in **Figure 6a** and Figure 2c, preliminarily indicating that the LATP has not been invaded by the polysulfide species. To further confirm this, the cycled PIN-LATP was characterized with small angle x-ray scattering (SAXS). The result is presented in Figure 6b. It has been reported that the peaks of polysulfide species usually appear at a 2-theta range of 1 to 2 degrees.^[23] However, as seen in Figure 6b, the SAXS pattern of the cycled PIN-LATP does not show any peaks within 1 to 2 degrees, attesting that no polysulfides has penetrated through the PIN to reach LATP. Figure 6c shows a SEM image of the cross-section of the cycled PIN-coated LATP after 150 cycles. There is no significant delamination phenomenon observed, revealing that the PIN coating is still well adhered on the surface of the LATP membrane after long-term cycling.

The cycled ((after 150 cycles in a Li || PIN-LATP || S/C cell) LATP membrane was also characterized with x-ray photoelectron spectroscopy (XPS). The sample was prepared by

meticulously removing the PIN coating from the LATP substrate. The XPS experiments were conducted on the side facing the S/C cathode. For a comparison, a piece of pristine LATP membrane was also analyzed. **Figure 7a** shows the survey-scan spectra of, respectively, a fresh LATP membrane and a cycled LATP. The two spectra exhibit identical peaks of carbon, lithium, aluminum, titanium, phosphorous, and oxygen, as expected. There is no sulfur signal in the cycled LATP membrane. The Ti 2p spectra of the two samples were particularly characterized, as presented in Figure 7b. In comparison to the spectrum of the fresh LATP, there is no peak shift in the Ti 2p spectrum of the cycled LATP, indicating that there is no reduction of Ti^{4+} has occurred. This result further confirms that there is no polysulfide invasion at the positive-electrode side during the operation of the $\text{Li} \parallel \text{PIN-LATP} \parallel \text{S/C}$ cell.

Figure 8 shows the SEM/EDS analysis results of a fresh LATP membrane and a cycled (after 150 cycles in a $\text{Li} \parallel \text{PIN-LATP} \parallel \text{S/C}$ cell) LATP membrane. The sample of the cycled LATP membrane was prepared in a similar way to that for the XPS experiment. The PIN coating was cautiously removed from the LATP substrate before the analysis. There is no sulfur peak observed in the EDS spectra (Figure 8a and b), implying that sulfur does not reach the surface of LATP membrane during cycling. The elemental mappings of the fresh and cycled LATP show no differences between the two samples (Figure 8d – h and Figure 8j - n), attesting that the SEM/EDS analysis results are consistent with the XPS analyses.

3. Conclusion

In summary, we have developed a new strategy for addressing the polysulfide-shuttle issues in lithium-sulfur batteries with a lithium-ion conductive solid electrolyte (LATP), which is coated with a layer of a polymer with intrinsic nanoporosity (PIN). The unique structure of PIN layer can efficaciously prevent the migration of polysulfide species, but allows the transport of Li^+ ions. At the anode, the PIN layer not only prevents the direct contact of Li-metal anode with LATP, but also the elastic feature of PIN enhances the ionic

interface between the two solid-phase materials (Li-metal and LATP ceramic). At the cathode, with its special structure, the PIN layer prevents the invasion of polysulfide species to the surface of LATP and meanwhile maintains an adequate ionic interface between the sulfur-carbon composite cathode and the LATP membrane. Therefore, the cycling stability of Li-S cells is greatly improved through the use of a PIN-LATP separator.

4. Experimental Section

Materials and Chemicals. $\text{Li}_{1+x}\text{Al}_x\text{Ti}_{2-x}(\text{PO}_4)_3$ (LATP) membranes were purchased from OHARA Inc., Japan. Carbon nanofiber (CNF) powder was purchased from Pyrograf Products Inc. Sulfur powder (S) was purchased from Acros Organics®. Chemicals for the synthesis of the polymer with intrinsic nanoporosity (PIN) include 5,5',6,6'-Tetrahydroxy-3,3,3',3'-tetramethyl-1,1'-spirobisindane (96%, Sigma Aldrich), cyclohexane (99%, Alfa Aesar), dimethylacetamide (DMAc, 99%, Sigma-Aldrich), tetrafluoroterephthalonitrile (99%, Sigma Aldrich), anhydrous K_2CO_3 (99%, Alfa Aesar), and tetrahydrofuran (THF, 99.9%, Sigma-Aldrich). Chemicals for the preparation of liquid electrolytes include lithium trifluoromethanesulfonate (LiCF_3SO_3 , Acros Organics®), dimethoxyethane (DME, Sigma Acros Organics®), and 1,3-dioxolane (DOL, Acros Organics®).

Synthesis of PIN material. To a three-necked flask, 2.72 g of tetrahydroxy-3,3,3',3'-tetramethyl-1,1'-spirobisindane, 2.21 g of K_2CO_3 , 15 mL of cyclohexane, and 30 mL of DMAc were added. The mixture was maintained at 110 °C for 3 h for dehydration. After the mixture was cooled down, 1.61 g of tetrafluoroterephthalonitrile and 25 mL of dimethylacetamide were added. The resulting mixture was maintained at 70 °C for 72 h to complete the polymerization reaction. Afterward, the mixture was cooled down and the PIN powder was collected. After being rinsed with deionized (DI)

water and methanol (3 times each), the PIN powder was dried under vacuum at 100 °C for 24 h.

Preparation of PIN-coated LATP. First the PIN powder was dispersed into tetrahydrofuran reagent to yield a 2.0 % solution. Then, the LATP membranes were dipped into the PIN/THF dispersion and settled for 5 min. Afterward, the LATP membranes were taken out of the PIN/THF dispersion and dried in a fume hood.

Preparation of cathode matrix and sulfur/carbon cathodes. A carbon nanofiber (CNF) paper was employed as the cathode matrix and current collector. The CNF paper was fabricated with CNF powder through a dispersion-filtration process.^[12a, 12b] The CNF powder was first dispersed into DI water to render a CNF slurry. Then, the CNF slurry was poured onto a piece of filter paper. After the filtration process, a layer of uniform CNF paper formed on the filter paper. Then, the CNF paper was rinsed with DI water and ethanol. After being dried (under vacuum at ~ 50 °C), the CNF paper was peeled off the filter paper.

For the coin cell preparation, circular CNF disks with a diameter 1.2 cm were punched out of the CNF paper. The area of the CNF electrode matrix was 1.13 cm² with a thickness of 40 – 50 μm. The liquid electrolyte was prepared by dissolving 1.0 M LiCF₃SO₃ in a DME-DOL (1 : 1, v : v) mixture solvent (LiCF₃SO₃/DME-DOL). The sulfur/CNF cathodes were prepared by dispersing a slurry of the sulfur powder and LiCF₃SO₃/DME-DOL electrolyte onto the CNF paper. The sulfur loading in the CNF cathode matrix was maintained at ~ 3.0 mg cm⁻².

Coin cell assembly and testing. The Li-S coin cells were assembled inside an Ar-filled glove box, as schematized in Figure S5 and Figure S9. First, a sulfur/CNF disk

electrode (with a diameter 1.2 cm and an area 1.13 cm²) was placed in the cell can. Then, a piece of uncoated LATP membrane, or a piece of PIN-LATP membrane, or a piece of Celgard separator was placed on top of the sulfur/CNF electrode. Then, 5 μ L of the LiCF₃SO₃/DME-DOL electrolyte was spread onto the top of the separator membrane. Next, a Li-foil disc (with a diameter 1.55 cm and an area 1.88 cm²) was placed on the top of the separator. The weight of the Li foil is *ca.* 50 mg. According to the practically delivered capacity of the cell, the amount of Li metal stripped from the anode upon a full discharge is about 1.0 mg. Therefore, the amount of lithium-metal anode is excess in the cells. Finally, the coin cells were sealed inside the glove box. The uncoated LATP membrane, PIN-coated LATP membrane, and Celgard separator was pre-soaked with the LiCF₃SO₃/DME-DOL electrolyte for 24 h prior to the cell assembly. Li-Li symmetric cells were prepared in the same manner with a piece of Li foil on either side of the membrane (*i.e.*, both as anode and cathode), as schematized in Figure S3. 5 μ L of the LiCF₃SO₃/DME-DOL electrolyte was applied to either side of the membrane.

Electrochemical performances of the Li-S coin cells were tested with a BT2000 Arbin® instrument. Cyclic voltammetry (CV) experiments were also conducted on the BT2000 Arbin® cycler. The scan rate for CV experiments was 0.05 mV s⁻¹. The electrochemical impedance spectroscopy (EIS) measurements were conducted on a Solartron® 1287 potentiostat from 10⁶ to 10⁻¹ Hz.

Analysis and characterization. Scanning electron microscope (SEM) experiments were conducted on a FEI Quanta 650 instrument. The elemental mapping results were examined with an EDS attached to the FEI Quanta 650 SEM. X-ray diffraction (XRD) measurements were performed with a Rigaku Ultima IV diffractometer (Cu K α radiation, λ = 0.15405 nm, step width of 0.02°, 4 s counting time per step). Non-contact profilometry experiments were

performed with a Veeco DEKTAK 150 profilometer. Fourier transform infrared spectra (FTIR) experiments were conducted on a Nicolet IS5 FTIR spectrometer. ^1H NMR analysis of the PIN material (with CDCl_3 solvent) was conducted at room temperature on a 500 MHz Agilent MR spectrometer. A Xenocs Ganesha small angle scattering instrument fitted with a moveable Dectris 300k detector was used to record medium angle ($2\text{-theta} < 9^\circ$) scattering data. The instrument is fitted with a microfocus Cu k-alpha source operated at 50 kV and 0.6 mA. A manufacturer supplied utility, SAXSGUI, was used to make the corrections and reduce the 2D detector data into intensity vs. scattering angle data. X-ray photoelectron spectroscopy (XPS) experiments were conducted on a Kratos AXIS Supra (XPS) surface analysis instrument.

Supporting Information

Supporting Information is available from the Wiley Online Library or from the author.

Acknowledgements

This work was supported by the U.S. Department of Energy, Office of Basic Energy Sciences, Division of Materials Sciences and Engineering under award number DE-SC0005397. The authors also thank Mr. Steve Swinnea and Mr. Robert Pipes for their assistance, respectively, with the SAXS and NMR experiments.

Received: ((will be filled in by the editorial staff))

Revised: ((will be filled in by the editorial staff))

Published online: ((will be filled in by the editorial staff))

- [1] aA. Manthiram, X. W. Yu, S. Wang, *Nat Rev Mater* **2017**, *2*, 16103; bM. Armand, J. M. Tarascon, *Nature* **2008**, *451*, 652-657; cA. Kwade, W. Haselrieder, R. Leithoff, A. Modlinger, F. Dietrich, K. Droeder, *Nature Energy* **2018**, *3*, 290-300.
- [2] aW. D. Li, B. H. Song, A. Manthiram, *Chem Soc Rev* **2017**, *46*, 3006-3059; bX. W. Yu, A. Manthiram, *Energ Environ Sci* **2018**, *11*, 527-543.
- [3] aM. S. Whittingham, *Chem Rev* **2004**, *104*, 4271-4301; bY. M. Sun, N. A. Liu, Y. Cui, *Nature Energy* **2016**, *1*, 16071.
- [4] aA. Manthiram, Y. Z. Fu, S. H. Chung, C. X. Zu, Y. S. Su, *Chem Rev* **2014**, *114*, 11751-11787; bQ. Pang, X. Liang, C. Y. Kwok, L. F. Nazar, *Nature Energy* **2016**, *1*, 16132; cX. W. Yu, A. Manthiram, *Accounts Chem Res* **2017**, *50*, 2653-2660.
- [5] aS. H. Chung, A. Manthiram, *Adv Funct Mater* **2014**, *24*, 5299-5306; bJ. X. Song, T. Xu, M. L. Gordin, P. Y. Zhu, D. P. Lv, Y. B. Jiang, Y. S. Chen, Y. H. Duan, D. H.

- Wang, *Adv Funct Mater* **2014**, *24*, 1243-1250; cA. Manthiram, Y. Z. Fu, Y. S. Su, *Accounts Chem Res* **2013**, *46*, 1125-1134.
- [6] aY. S. Su, Y. Z. Fu, T. Cochell, A. Manthiram, *Nat Commun* **2013**, *4*, 3985; bA. Manthiram, S. H. Chung, C. X. Zu, *Adv Mater* **2015**, *27*, 1980-2006; cY. Z. Fu, Y. S. Su, A. Manthiram, *Angew Chem Int Edit* **2013**, *52*, 6930-6935.
- [7] aH. J. Peng, J. Q. Huang, X. B. Cheng, Q. Zhang, *Adv Energy Mater* **2017**, *7*, 1700260; bG. R. Li, S. Wang, Y. N. Zhang, M. Li, Z. W. Chen, J. Lu, *Adv Mater* **2018**, *30*, 1705590; cR. P. Fang, S. Y. Zhao, Z. H. Sun, W. Wang, H. M. Cheng, F. Li, *Adv Mater* **2017**, *29*, 1606823.
- [8] aX. W. Yu, Z. H. Bi, F. Zhao, A. Manthiram, *Acs Appl Mater Inter* **2015**, *7*, 16625-16631; bX. W. Yu, Z. H. Bi, F. Zhao, A. Manthiram, *Adv Energy Mater* **2016**, *6*, 1601392.
- [9] aD. N. Lei, K. Shi, H. Ye, Z. P. Wan, Y. Y. Wang, L. Shen, B. H. Li, Q. H. Yang, F. Y. Kang, Y. B. He, *Adv Funct Mater* **2018**, *28*, 1707570; bY. Z. Sun, J. Q. Huang, C. Z. Zhao, Q. Zhang, *Sci China Chem* **2017**, *60*, 1508-1526.
- [10] aJ. Hassoun, B. Scrosati, *Adv Mater* **2010**, *22*, 5198-5201; bA. Hayashi, T. Ohtomo, F. Mizuno, K. Tadanaga, M. Tatsumisago, *Electrochem Commun* **2003**, *5*, 701-705; cA. Hayashi, R. Ohtsubo, T. Ohtomo, F. Mizuno, M. Tatsumisago, *J Power Sources* **2008**, *183*, 422-426.
- [11] aT. Kobayashi, Y. Imade, D. Shishihara, K. Homma, M. Nagao, R. Watanabe, T. Yokoi, A. Yamada, R. Kanno, T. Tatsumi, *J Power Sources* **2008**, *182*, 621-625; bM. Nagao, Y. Imade, H. Narisawa, T. Kobayashi, R. Watanabe, T. Yokoi, T. Tatsumi, R. Kanno, *J Power Sources* **2013**, *222*, 237-242.
- [12] aX. W. Yu, J. Joseph, A. Manthiram, *J Mater Chem A* **2015**, *3*, 15683-15691; bX. W. Yu, J. Joseph, A. Manthiram, *Mater Horiz* **2016**, *3*, 314-319; cX. W. Yu, A. Manthiram, *Phys Chem Chem Phys* **2015**, *17*, 2127-2136.
- [13] aL. Wang, Y. G. Wang, Y. Y. Xia, *Energ Environ Sci* **2015**, *8*, 1551-1558; bQ. S. Wang, J. Jin, X. W. Wu, G. Q. Ma, J. H. Yang, Z. Y. Wen, *Phys Chem Chem Phys* **2014**, *16*, 21225-21229; cX. L. Wu, J. Zong, H. Xu, W. Wang, X. J. Liu, *Rsc Adv* **2016**, *6*, S7346-S7356.
- [14] aC. W. Sun, J. Liu, Y. D. Gong, D. P. Wilkinson, J. J. Zhang, *Nano Energy* **2017**, *33*, 363-386; bX. Judez, H. Zhang, C. M. Li, G. G. Eshetu, J. A. Gonzalez-Marcos, M. Armand, L. M. Rodriguez-Martinez, *J Electrochem Soc* **2018**, *165*, A6008-A6016; cK. Kerman, A. Luntz, V. Viswanathan, Y. M. Chiang, Z. B. Chen, *J Electrochem Soc* **2017**, *164*, A1731-A1744.
- [15] aS. F. Wang, H. H. Xu, W. D. Li, A. Dolocan, A. Manthiram, *J Am Chem Soc* **2018**, *140*, 250-257; bS. F. Wang, Y. Ding, G. M. Zhou, G. H. Yu, A. Manthiram, *Acs Energy Letters* **2016**, *1*, 1080-1085.
- [16] aY. T. Li, W. D. Zhou, X. Chen, X. J. Lu, Z. M. Cui, S. Xin, L. G. Xue, Q. X. Jia, J. B. Goodenough, *P Natl Acad Sci USA* **2016**, *113*, 13313-13317; bW. D. Zhou, S. F. Wang, Y. T. Li, S. Xin, A. Manthiram, J. B. Goodenough, *J Am Chem Soc* **2016**, *138*, 9385-9388.
- [17] X. W. Yu, S. N. Feng, M. J. Boyer, M. Lee, R. C. Ferrier, N. A. Lynd, G. S. Hwang, G. B. Wang, S. Swinnea, A. Manthiram, *Materials Today Energy* **2018**, *7*, 98-104.
- [18] H. Ishida, *Interfaces in polymer, ceramic, and metal matrix composites*, Elsevier, New York, USA **1988**.
- [19] Y. Meesala, A. Jena, H. Chang, R. S. Liu, *Acs Energy Letters* **2017**, *2*, 2734-2751.
- [20] aY. S. Su, A. Manthiram, *Nat Commun* **2012**, *3*, 1166; bJ. Q. Huang, Q. Zhang, F. Wei, *Energy Storage Mater* **2015**, *1*, 127-145.
- [21] aX. W. Yu, A. Manthiram, *Adv Energy Mater* **2015**, *5*, 1500350; bX. W. Yu, A. Manthiram, *Energy Storage Mater* **2018**, *15*, 368-373.

- [22] aC. X. Zu, L. J. Li, J. H. Guo, S. F. Wang, D. L. Fan, A. Manthiram, *J Phys Chem Lett* **2016**, 7, 1392-1399; bC. X. Zu, A. Dolocan, P. H. Xiao, S. Stauffer, G. Henkelman, A. Manthiram, *Adv Energy Mater* **2016**, 6, 1501933.
- [23] aJ. Nelson, S. Misra, Y. Yang, A. Jackson, Y. J. Liu, H. L. Wang, H. J. Dai, J. C. Andrews, Y. Cui, M. F. Toney, *J Am Chem Soc* **2012**, 134, 6337-6343; bG. Q. Tan, R. Xu, Z. Y. Xing, Y. F. Yuan, J. Lu, J. G. Wen, C. Liu, L. Ma, C. Zhan, Q. Liu, T. P. Wu, Z. L. Jian, R. Shahbazian-Yassar, Y. Ren, D. J. Miller, L. A. Curtiss, X. L. Ji, K. Amine, *Nature Energy* **2017**, 2, 17090.

Table 1. Specific discharge capacity, charge voltage, discharge voltage, and voltage gap of the Li || PIN-LATP || S/C and Li || Celgard || S/C cells at different cycling rates. The charge and discharge voltages are determined at the charge/discharge capacity of 500 mA h g⁻¹. The data are derived from the voltage profiles in Figure 4b and Figure S7.

	Li PIN-LATP S/C cell				Li Celgard S/C cell			
	C/10	C/5	C/3	C/2	C/10	C/5	C/3	C/2
Specific capacity, mA h g ⁻¹	1110	950	850	750	1230	1170	1080	1010
Charge voltage, V	2.35	2.48	2.62	2.83	2.27	2.28	2.33	2.36
Discharge voltage, V	1.99	1.87	1.73	1.54	2.07	2.05	2.03	1.99
Voltage gap, V	0.36	0.61	0.89	1.29	0.20	0.23	0.30	0.37

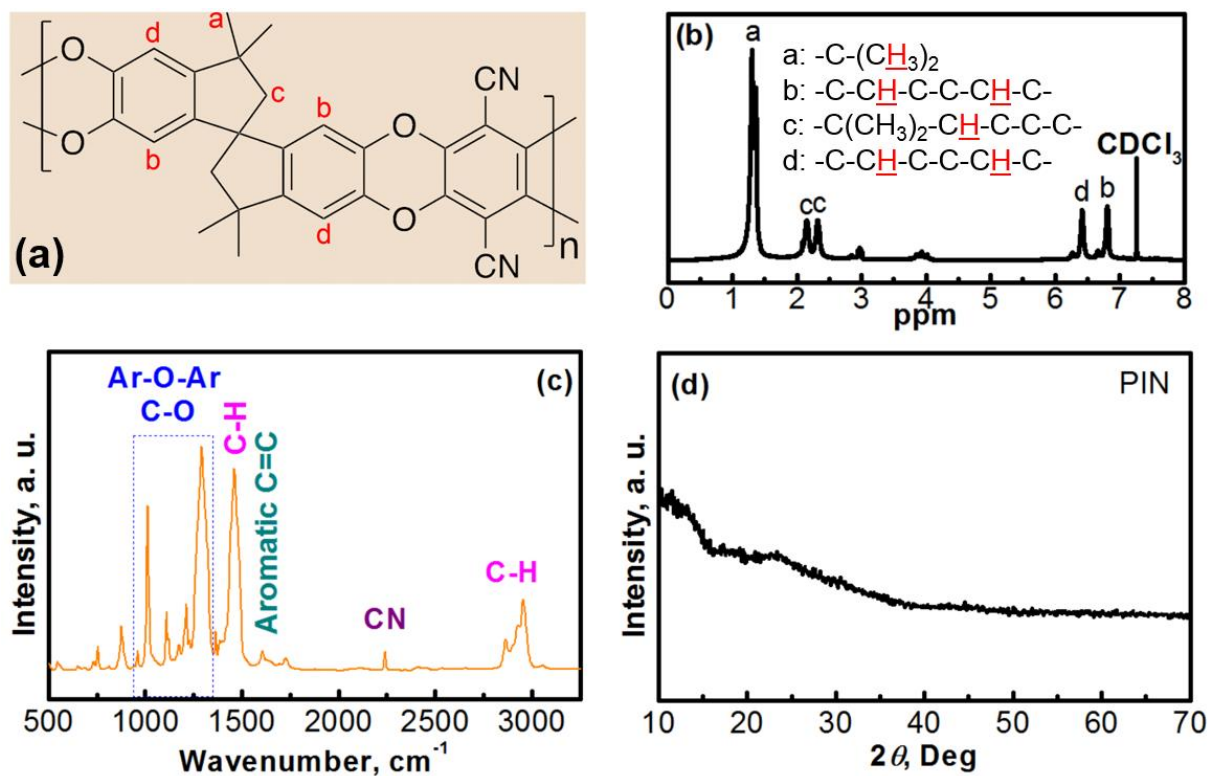


Figure 1. (a) Molecular structure of a polymer with intrinsic nanoporosity (PIN). (b) ^1H NMR spectrum of the PIN polymer. The labels correspond to the polymer structure in (a) and to their respective peaks in (b). (c) Fourier transform infrared (FTIR) spectrum of the PIN material. (d) X-ray diffraction (XRD) pattern of the PIN material.

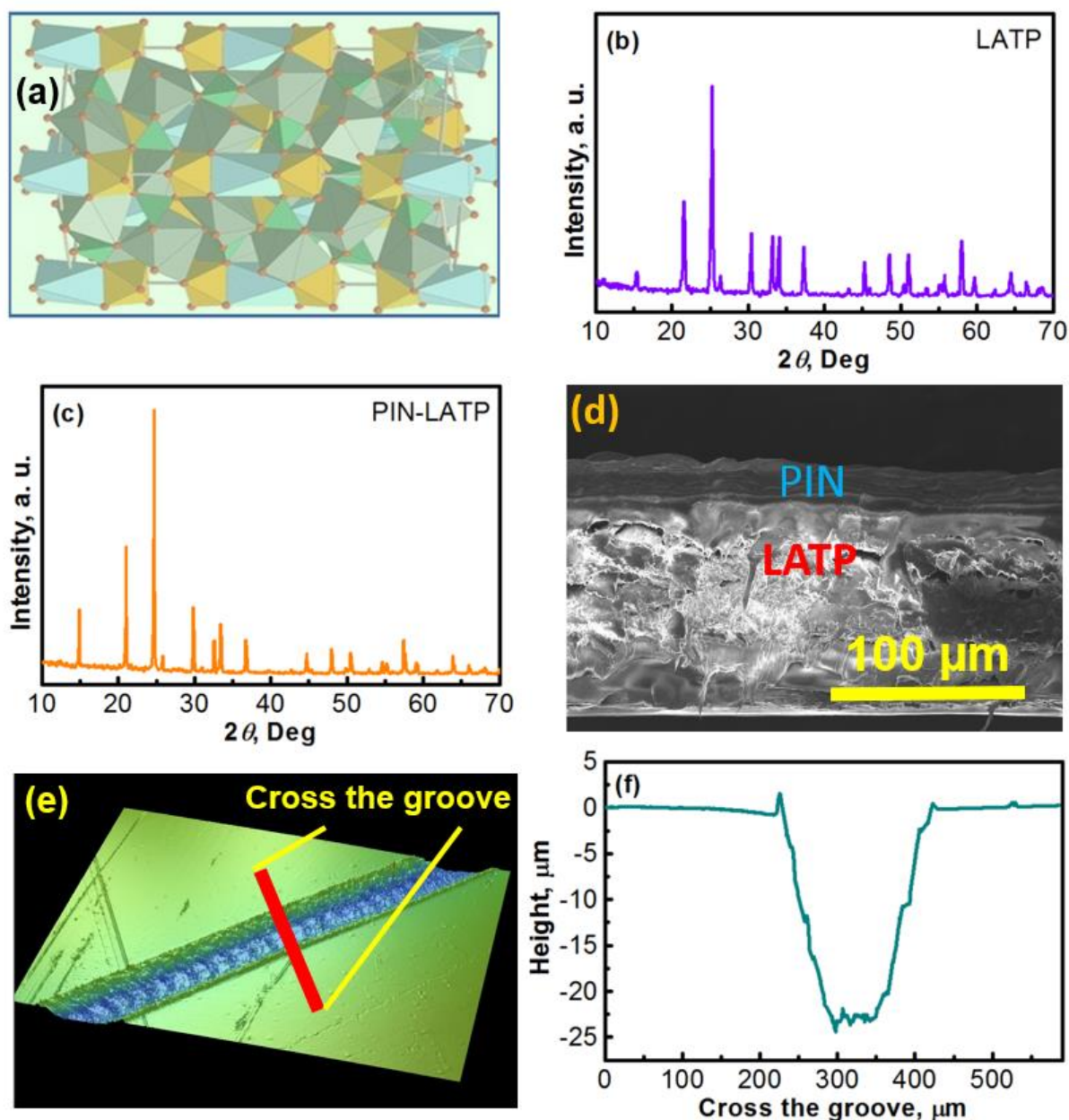


Figure 2. (a) Illustration of the NASICON structure of a $\text{Li}_{1+x}\text{Al}_x\text{Ti}_{2-x}(\text{PO}_4)$ (LATP) membrane. (b) XRD pattern of the LATP membrane. (c) XRD pattern of a PIN-coated LATP membrane. (d) Scanning electron microscope (SEM) image of the cross-section of a PIN-coated LATP membrane. (e) 3D noncontact profilometer pattern of an intentionally scratched PIN-coated LATP membrane. The blue groove is the LATP substrate. The yellow-green area is the PIN coating. (f) Profilometer depth profile across the scratched groove (as indicated in (g)) of the PIN-coated LATP membrane.

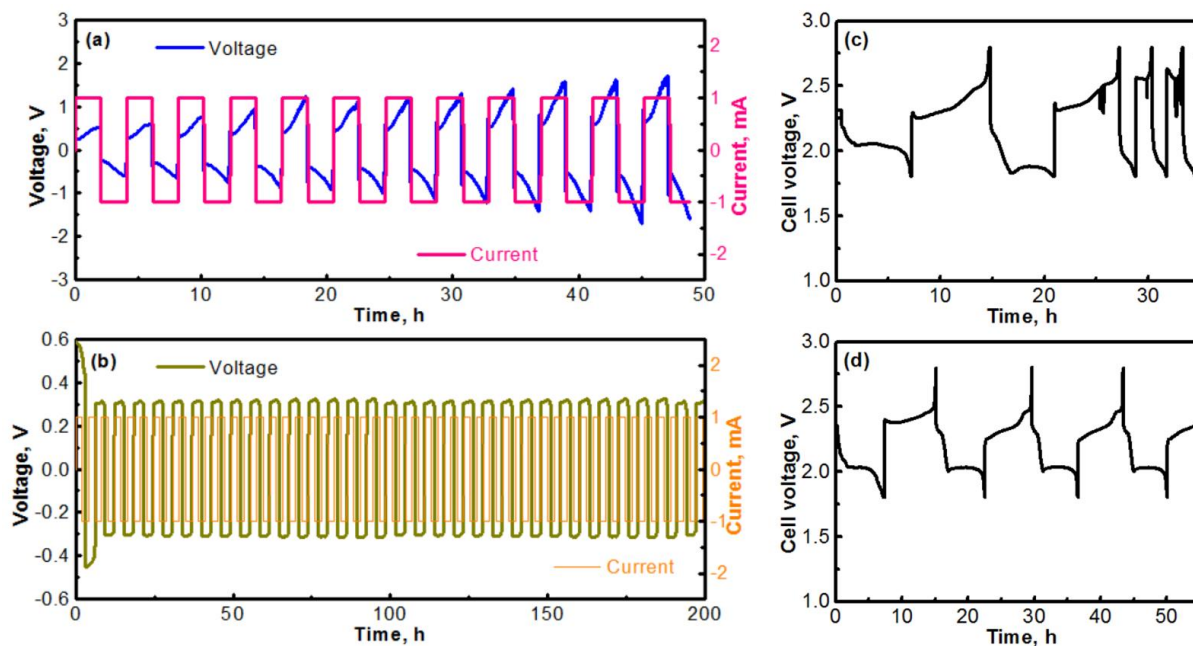


Figure 3. (a) Voltage and current profiles of a Li || LATP || Li symmetric cell prepared with an uncoated LATP membrane. (b) Voltage and current profiles of a Li || PIN-LATP || Li symmetric cell prepared with a PIN-coated LATP membrane. (c) Charge-discharge profile of a Li || LATP || S/C cell at the first few cycles. The cell was prepared with an uncoated LATP membrane. (d) Charge-discharge profile of a Li || PIN-LATP || S/C cell at the first few cycles. The cell was prepared with a PIN-coated LATP membrane.

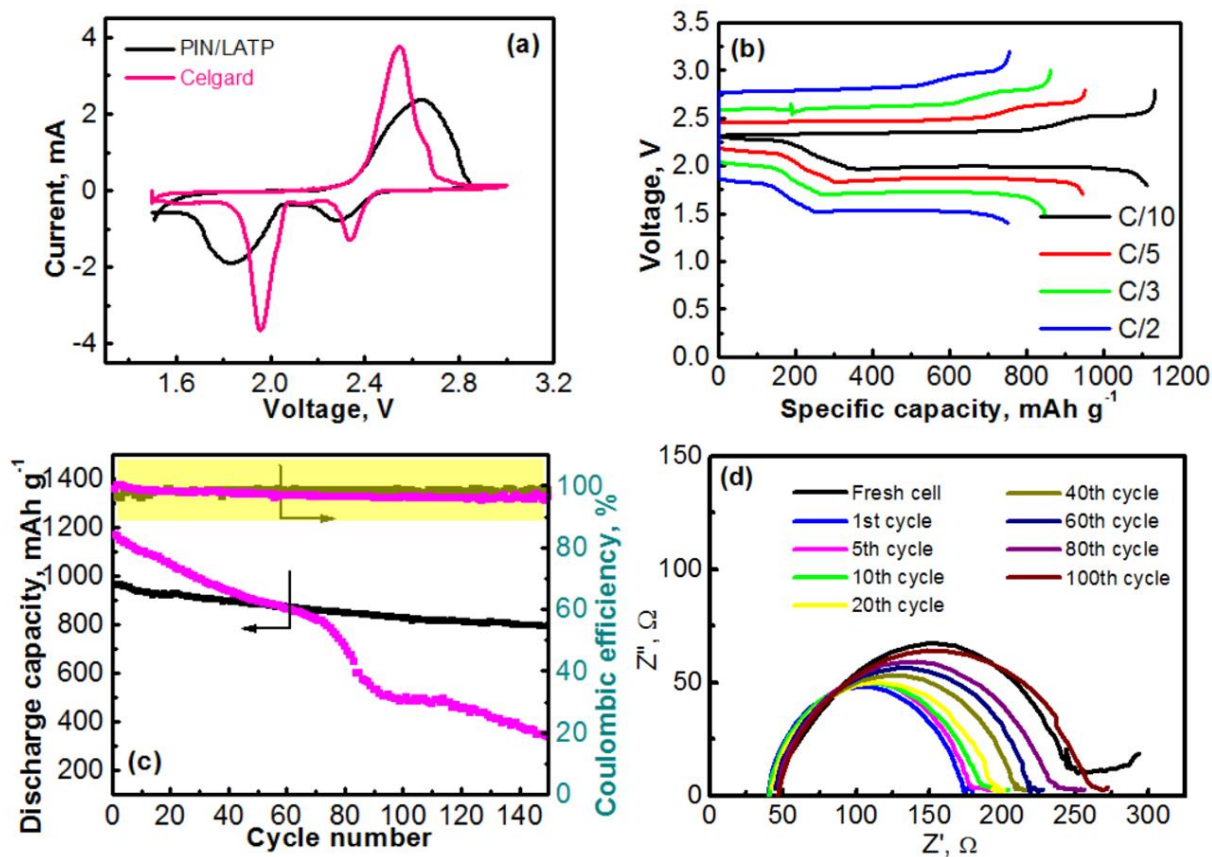


Figure 4. (a) Cyclic voltammogram (CV) curves of a Li || PIN-LATP || S/C cell and a Li || Celgard || S/C cell with a scan rate of 0.05 mV s⁻¹. (b) Charge-discharge curves of the Li || PIN-LATP || S/C cell at various C rates. (c) Specific discharge capacities as well as Coulombic efficiencies versus cycling numbers for the Li || PIN-LATP || S/C cell and the Li || Celgard || S/C cell at a cycling rate of C/5. (d) Electrochemical impedance spectroscopy (EIS) plots of a Li || PIN-LATP || S/C cell after being cycled for different number of cycles.

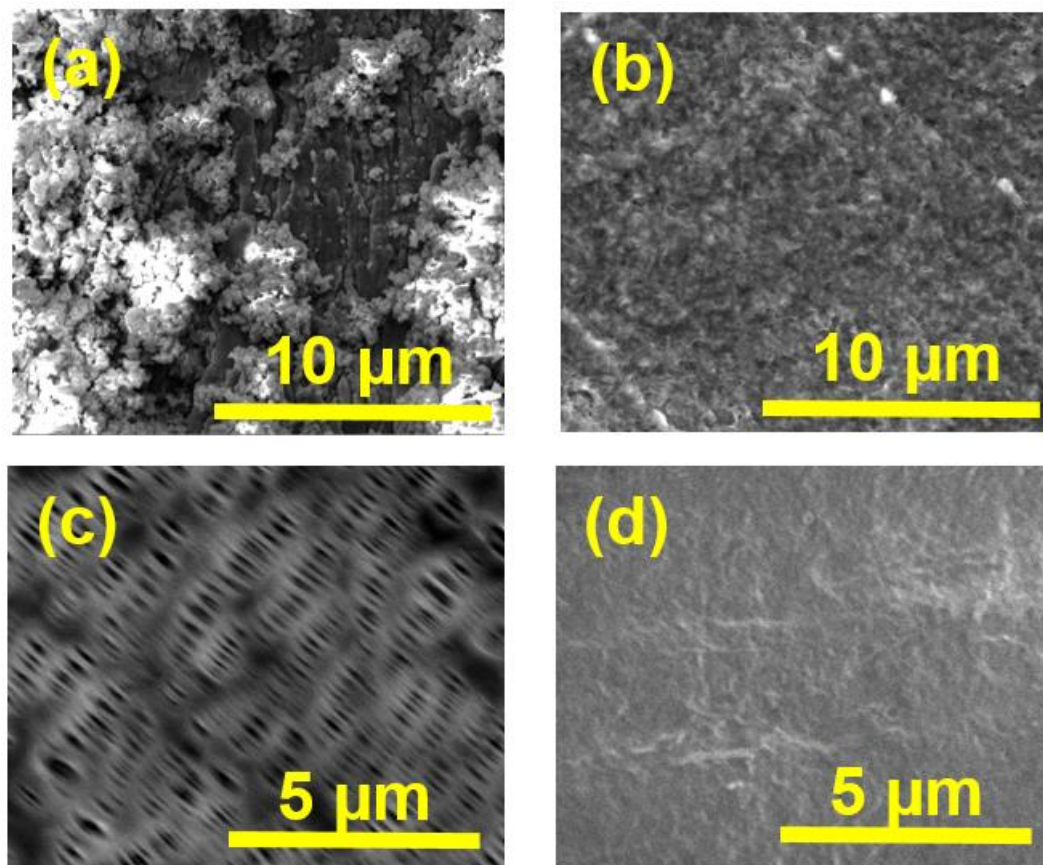


Figure 5. (a) Scanning electron microscope (SEM) image of a Li-metal anode taken from a cycled (after 150 cycles) Li || Celgard || S/C cell. (b) SEM image of a Li-metal anode taken from a cycled (after 150 cycles) Li || PIN-LATP || S/C cell. (c) SEM image of a piece of Celgard membrane. (d) SEM image of the PIN coating on a piece of LATP membrane.

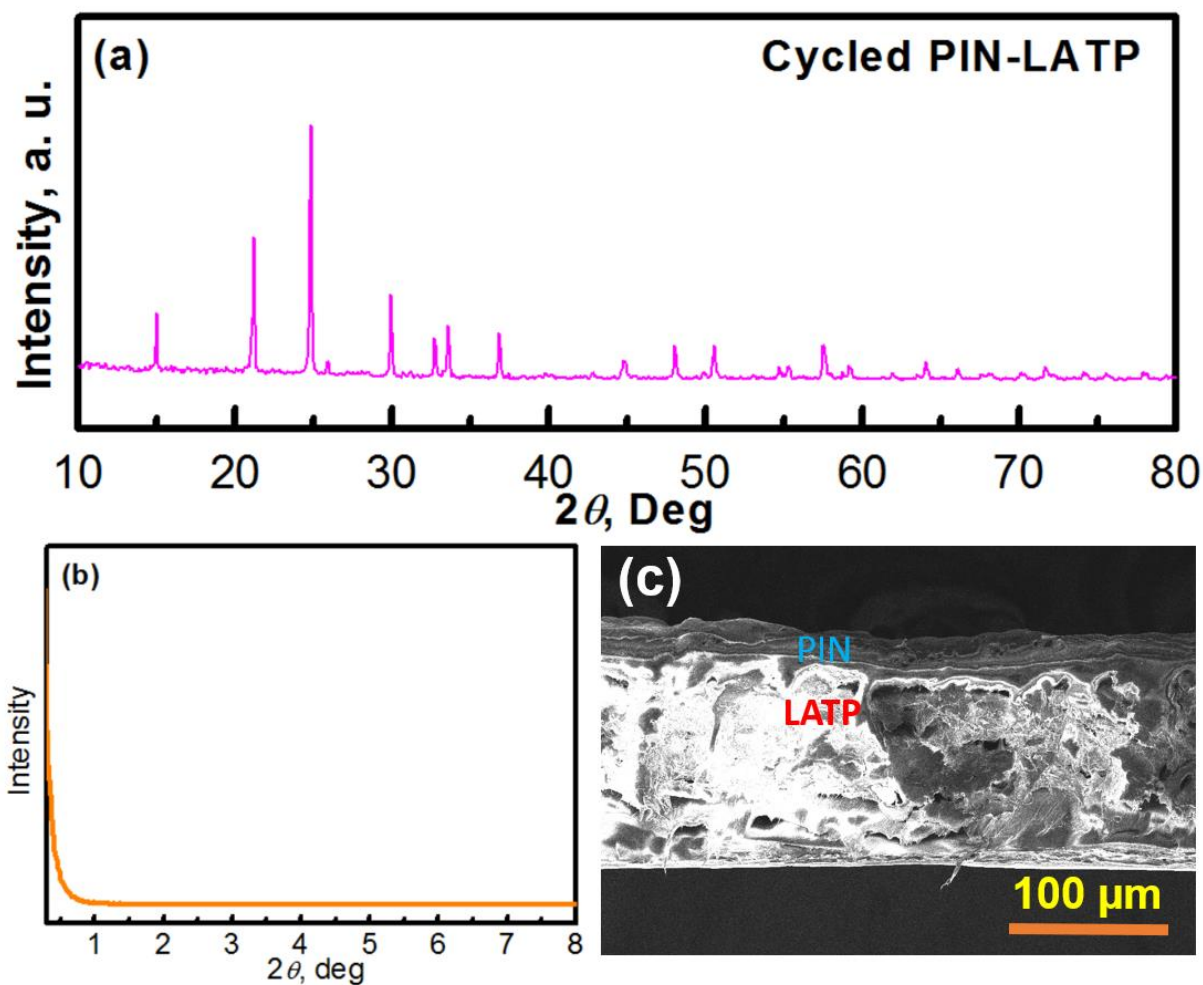


Figure 6. (a) XRD pattern of a cycled (after 150 cycles) PIN-LATP membrane taken from a cycled Li || PIN-LATP || S/C cell. (b) Small angle x-ray scattering (SAXS) pattern of the cycled (after 150 cycles) PIN-LATP membrane. (c) Scanning electron microscope (SEM) image of the cross-section of the cycled (after 150 cycles) PIN-LATP membrane.

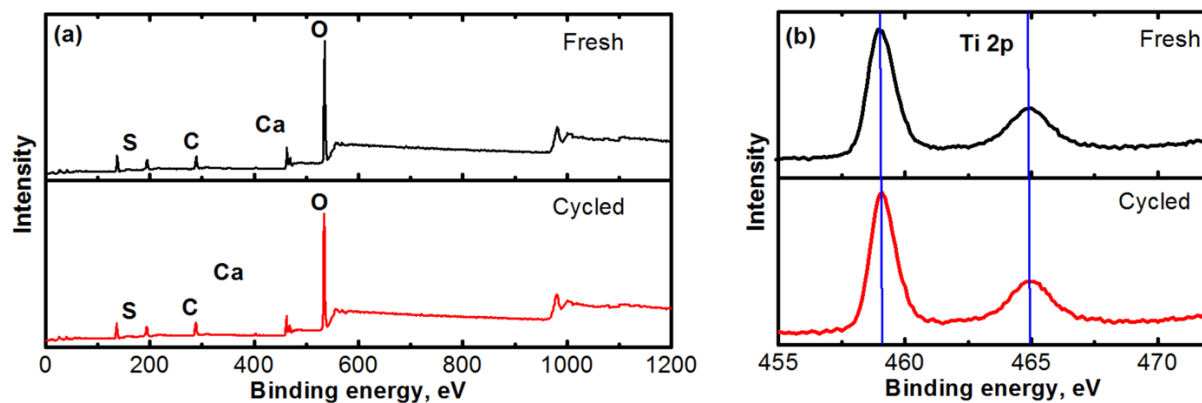


Figure 7. (a) XPS survey spectra of LATP membranes. Top: Fresh LATP membrane; bottom: cycled (after 150 cycles) LATP membrane taken from a cycled Li || PIN-LATP || S/C cell. (b) XPS Ti 2p spectra of LATP membranes. Top: Fresh LATP membrane; bottom: cycled (after 150 cycles) LATP membrane taken from a cycled Li || PIN-LATP || S/C cell.

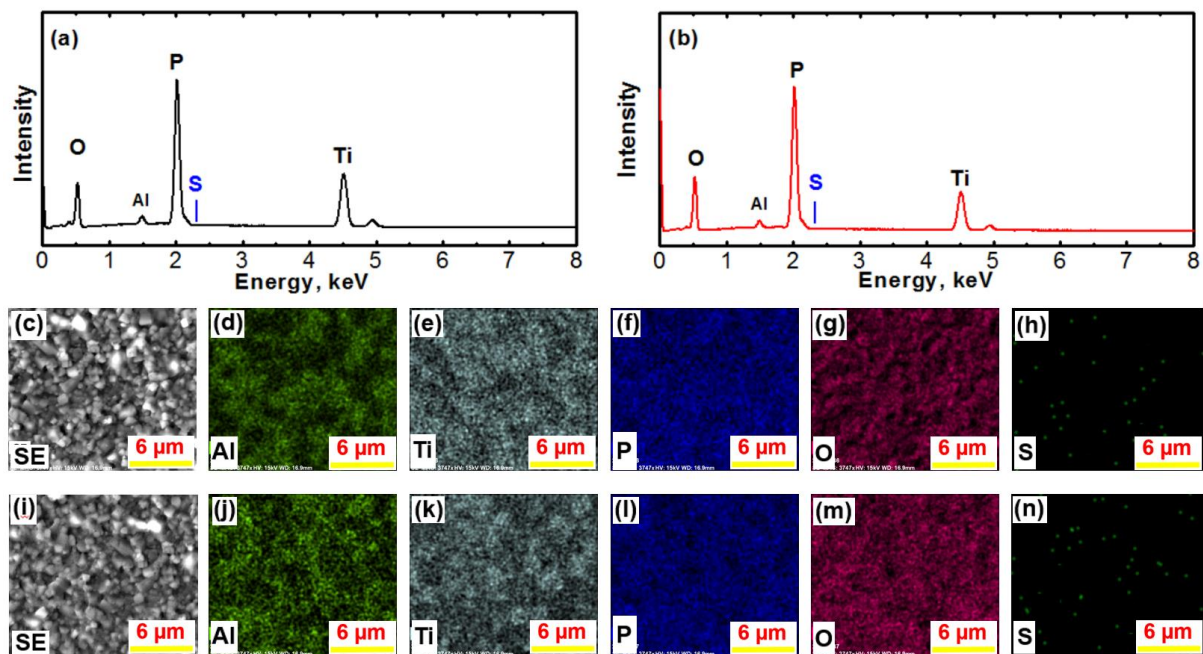


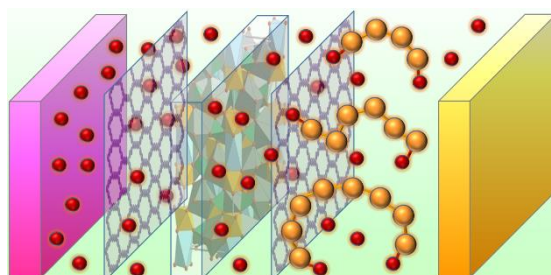
Figure 8. (a, b) Energy dispersive x-ray spectroscopy (EDS) of a fresh LATP membrane (a) and a cycled (after 150 cycles in a Li || PIN-LATP || S/C cell) LATP membrane (b). (c, i) Scanning electron microscope (SEM) images of the fresh LATP membrane (c) and a cycled (after 150 cycles in a Li || PIN-LATP || S/C cell) LATP membrane (i). (d - h) Elemental mappings obtained with EDS of a fresh LATP membrane. (j - n) Elemental mappings obtained with EDS of a cycled (after 150 cycles in a Li || PIN-LATP || S/C cell) LATP membrane. The analyzed elements are as indicated in (d - h), and (j - n).

A series of interfacial issues of a solid-electrolyte Li-S battery are addressed by employing a thin layer of a polymer with intrinsic nanoporosity (PIN) on a solid-electrolyte membrane.

Keywords: lithium-sulfur batteries, solid electrolyte, polymer with intrinsic nanoporosity, electrode-electrolyte interface, lithium polysulfide

Xingwen Yu and Arumugam Manthiram*

Enhanced Interfacial Stability of Hybrid-Electrolyte Lithium-Sulfur Batteries with a Layer of Multifunctional Polymer with Intrinsic Nanoporosity



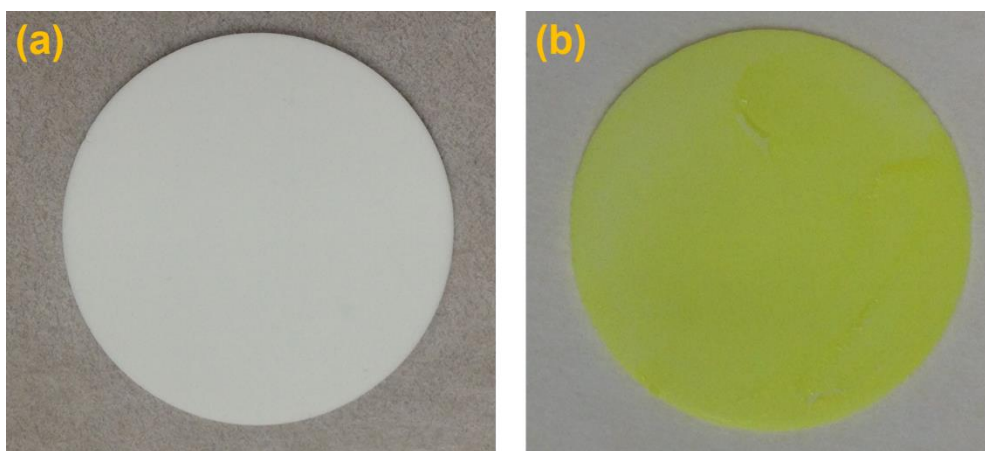
Enhanced Interfacial Stability of Hybrid-Electrolyte Lithium-Sulfur Batteries with a Layer of Multifunctional Polymer with Intrinsic Nanoporosity*Xingwen Yu and Arumugam Manthiram**

Figure S1. (a) Photo of a piece of $\text{Li}_{1+x}\text{Al}_x\text{Ti}_{2-x}(\text{PO}_4)_3$ (LATP) membrane. (b) Photo of a piece of polymer with intrinsic nanoporosity (PIN) that is coated onto a LATP membrane. The diameter of LATP pellet is 18 mm.

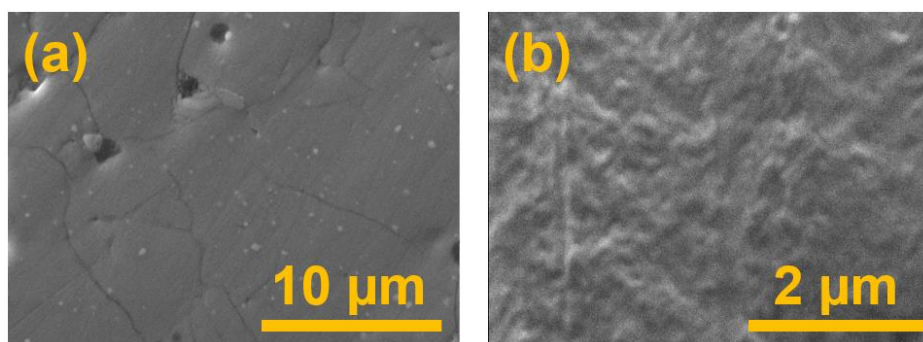


Figure S2. (a) SEM image of a piece of LATP membrane. (b) SEM image of a PIN-coated LATP membrane.

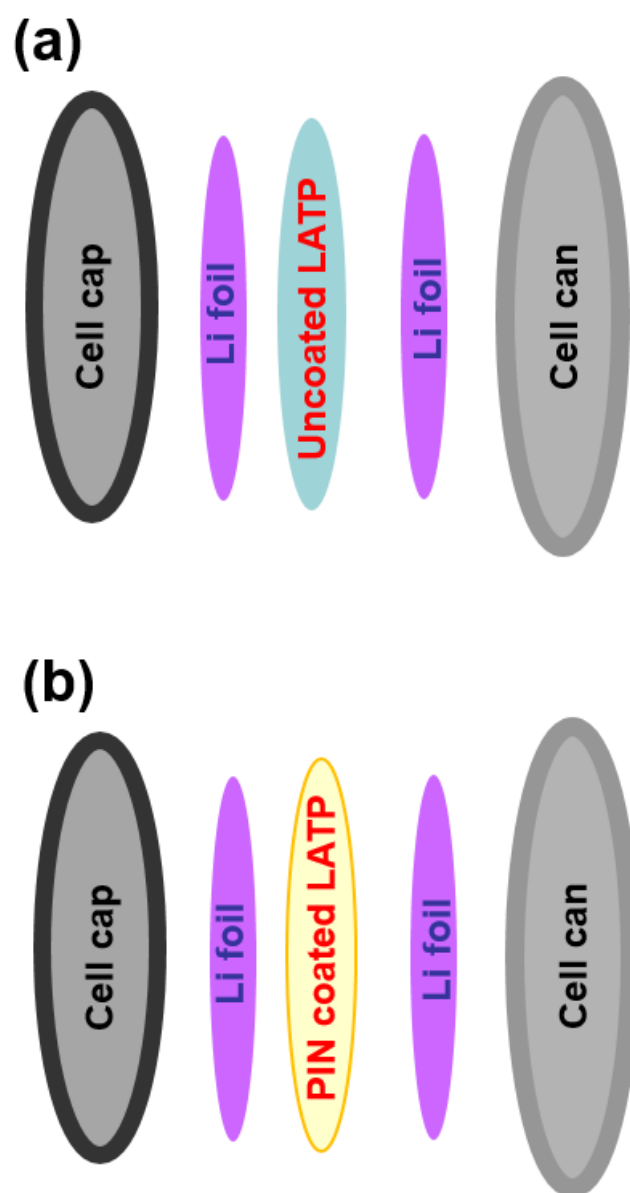


Figure S3. Schematics of a Li-Li symmetric coin cell with (a) an uncoated LAMP membrane and (b) a PIN-coated LAMP membrane.

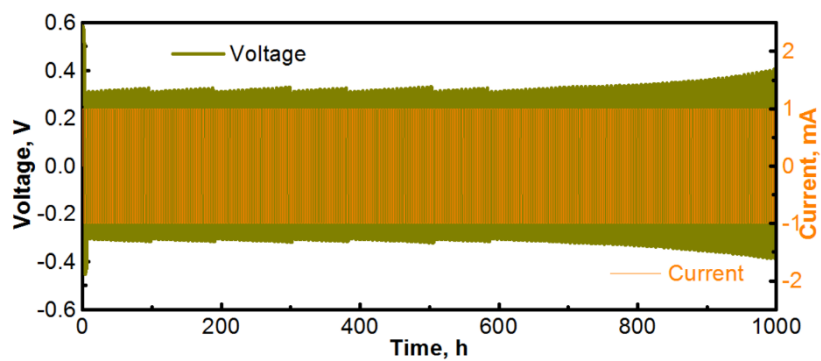


Figure S4. Voltage and current profiles of a Li || PIN-LATP || Li symmetric cell prepared with a PIN-coated LATP membrane.

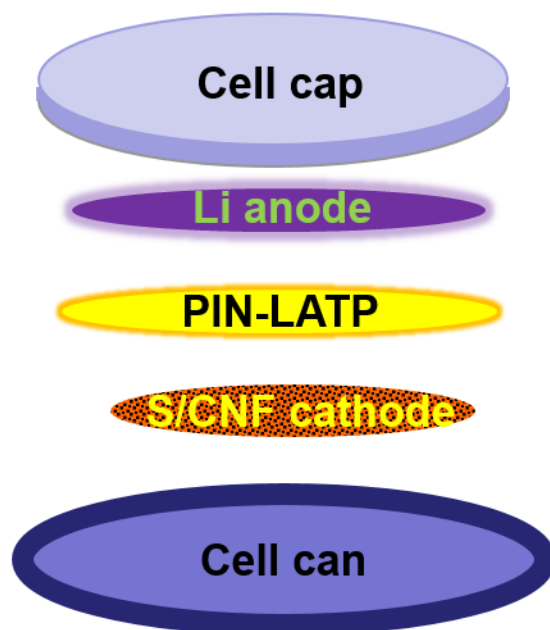


Figure S5. Schematic of the assembly of a Li-S coin cell with a PIN-LATP membrane, a CNF/S positive electrode, and a Li-foil negative electrode.

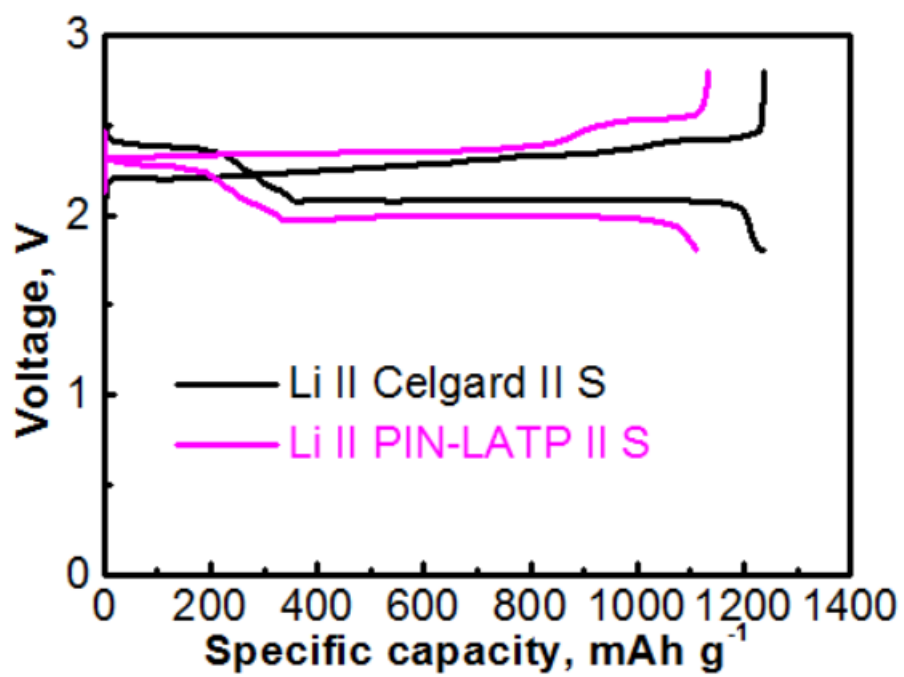


Figure S6. Charge-discharge curves of a Li || PIN-LATP || S/C cell and a Li || Celgard || S/C cell at a cycling rate of C/10.

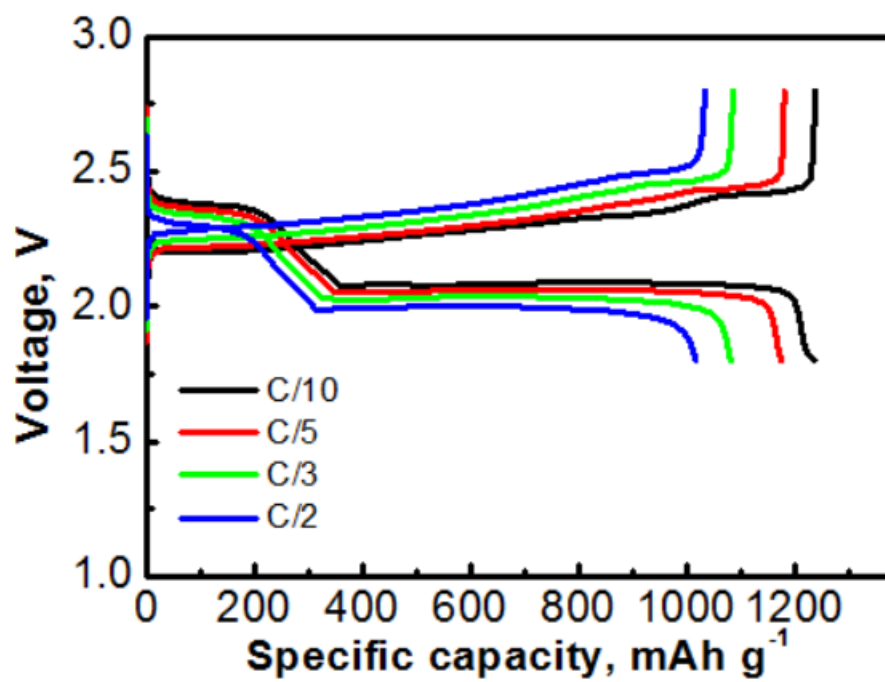


Figure S7. Charge-discharge curves of the Li || Celgard || S/C cells at various C rates.

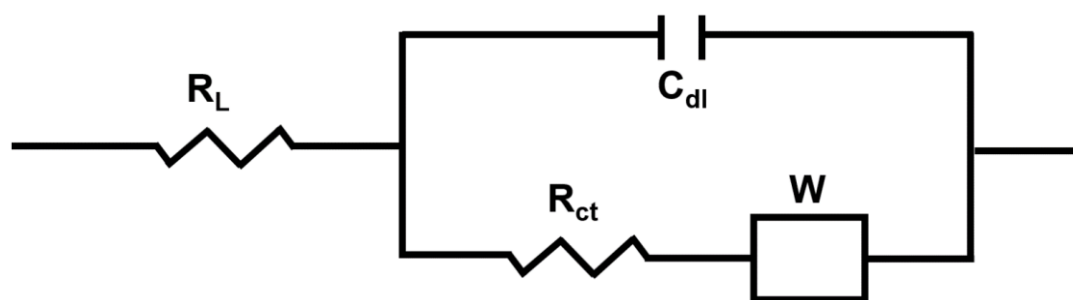


Figure S8. Equivalent circuit of the Li || PIN-LATP || S/C and Li || Celgard || S/C cells.

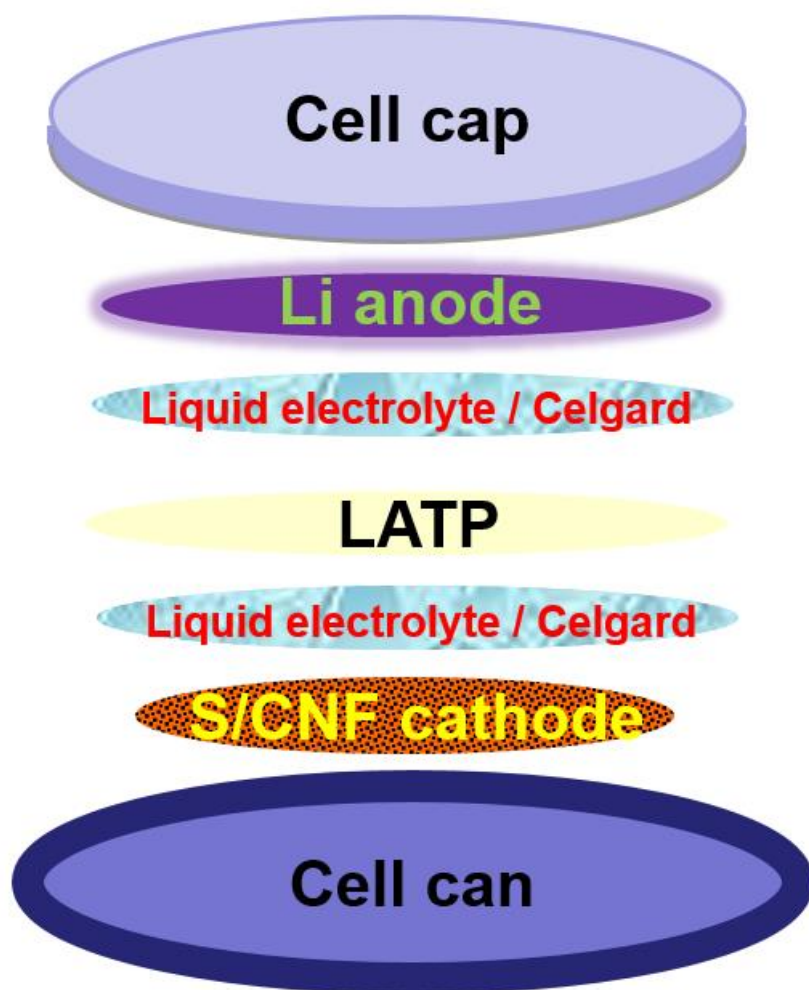


Figure S9. Schematic of the assembly of a Li-S coin cell with a LATP membrane, a CNF/S positive electrode, and a Li-foil negative electrode. A piece of liquid electrolyte ($\text{LiCF}_3\text{SO}_3/\text{DME-DOL}$) soaked Celgard membrane was placed in between the Li-foil anode and the LATP membrane as well as in between the LATP membrane and the CNF/S positive electrode.

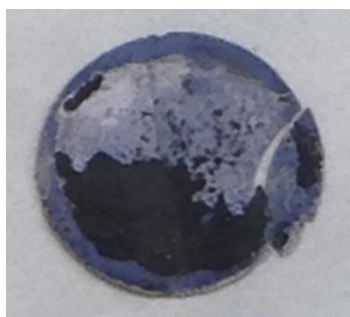


Figure S10. Photo of a piece of LATP membrane that has been cycled in a Li || Celgard-LATP || S/C cell for 30 cycles.



Figure S11. Photo of a piece of PIN-coated LATP after being cycled for 150 cycles in a Li || PIN-LATP || S/C cell.